HAL
open science

Charge-transfer driven by ultrafast spin-transition in a CoFe Prussian blue analogue

Marco Cammarata, Serhane Zerdane, Lodovico Balducci, Giovanni Azzolina, Sandra Mazerat, Cecile Exertier, Matilde Trabuco, Matteo Levantino, Roberto Alonso-Mori, James M Glownia, et al.

To cite this version:

Marco Cammarata, Serhane Zerdane, Lodovico Balducci, Giovanni Azzolina, Sandra Mazerat, et al.. Charge-transfer driven by ultrafast spin-transition in a CoFe Prussian blue analogue. Nature Chemistry, 2021, 13 (1), pp.10-14. 10.1038/s41557-020-00597-8 . hal-02996531

HAL Id: hal-02996531

https://hal.science/hal-02996531

Submitted on 9 Nov 2020

HAL is a multi-disciplinary open access archive for the deposit and dissemination of scientific research documents, whether they are published or not. The documents may come from teaching and research institutions in France or abroad, or from public or private research centers.

L'archive ouverte pluridisciplinaire **HAL**, est destinée au dépôt et à la diffusion de documents scientifiques de niveau recherche, publiés ou non, émanant des établissements d'enseignement et de recherche français ou étrangers, des laboratoires publics ou privés.

Charge-transfer driven by ultrafast spin-transition in a CoFe Prussian blue analogue

Marco Cammarata[1,*] Serhane Zerdane[1], Lodovico Balducci[1], Giovanni Azzolina[1], Sandra Mazerat[2], Cecile Exertier[3], Matilde Trabuco[3], Matteo Levantino[4], Roberto Alonso-Mori[5], James M. Glownia[5], Sanghoon Song[5], Laure Catala[2], Talal Mallah[2] , Samir F. Matar[6,7], Eric Collet[,1*]

*Email: eric.collet@univ-rennes1.fr and marco.cammarata@univ-rennes1.fr

[1]Univ Rennes, CNRS, IPR (Institut de Physique de Rennes) - UMR 6251, F-35000 Rennes, France.

[2] Institut de Chimie Moléculaire et des Matériaux d'Orsay, Université Paris-Sud, CNRS, Université Paris-Saclay, 91405 Orsay cedex, France.

[3] Department of Biochemical Sciences «A.R. Fanelli», Sapienza University of Rome, P.le A. Moro 5, 00185 Rome, Italy

[4] ESRF - The European Synchrotron, 71 Avenue des Martyrs, 38000 Grenoble, France

[5]Linac Coherent Light Source, SLAC National Accelerator Laboratory, Menlo Park, CA-94025, USA.

[6] ICMCB, CNRS UMR 5026, Université de Bordeaux, F-33600 Pessac, France.

[7]Lebanese German University (LGU), Sahel Alma Campus, PO Box 206, Jounieh, Lebanon

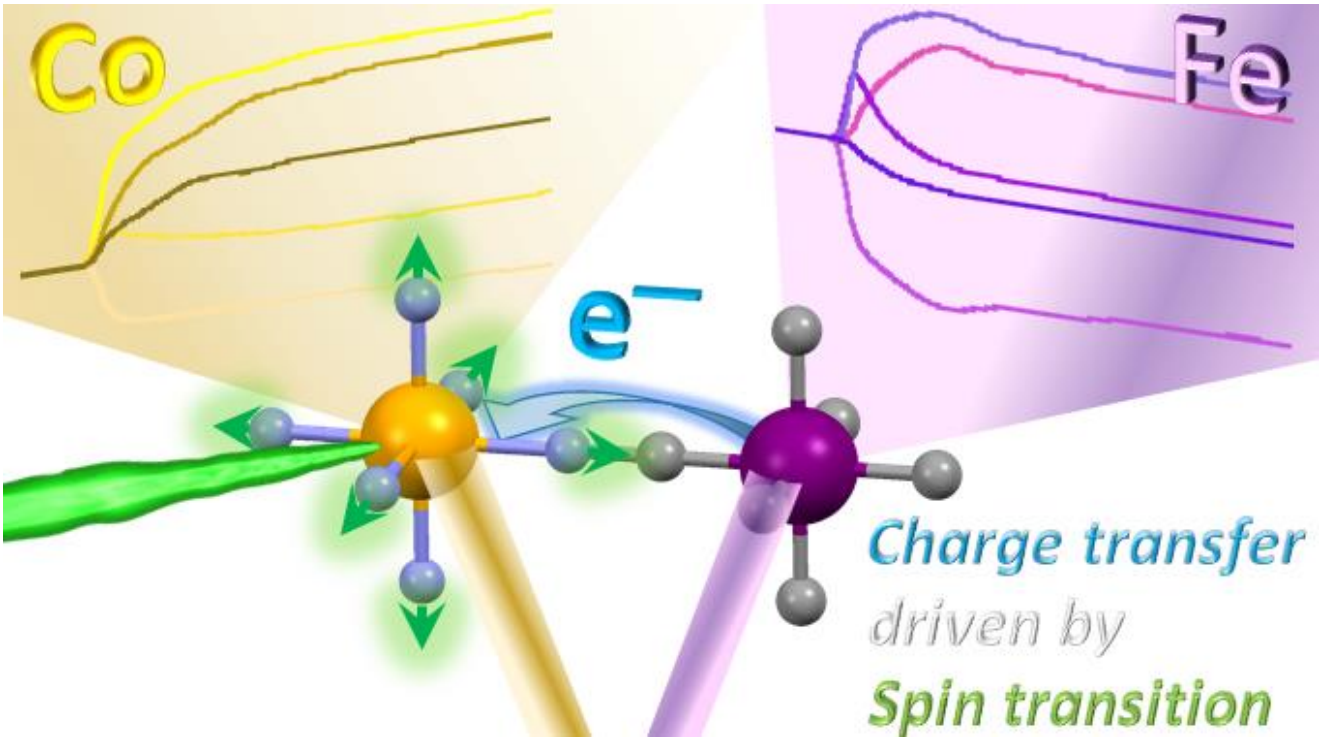

Abstract:

Photoinduced charge-transfer is an important process in nature and technology and is responsible for the emergence of exotic functionalities, such as magnetic order for cyanide-bridged bimetallic coordination networks. Despite its broad interest and intensive developments in chemistry and material sciences, the atomic-scale description of the initial photoinduced process, which couples intermetallic charge-transfer and spin-transition, has been debated for decades; it was beyond reach due to its extreme speed. Here we study this process in a prototype cyanide-bridged CoFe system by femtosecond X-ray and optical absorption spectroscopies, enabling the disentanglement of ultrafast electronic and structural dynamics. Our results demonstrate that it is the spin-transition that occurs first on the Co site within ≈50 fs, and it is this that drives the subsequent Fe-to-Co charge-transfer within ≈200 fs. This study represents a step towards understanding and controlling charge-transfer-based functions using light.

Main text

Photoinduced charge transfer (CT) is one of the primary events associated with the emergence of functions in nature and technology, found in various systems from simple dyads to proteins. Reported light-enabled functions are found to range from artificial solar energy conversion to photocatalysis [1,2] and to expand in materials towards magnetism [3-6], ferroelectricity [7] or conductivity [8]. Among different classes of multi-functional materials, cyanide-bridged bimetallic systems known as Prussian blue analogues (PBA) are very attractive, because the reversible CT between the constitutive transition metal ions is responsible for the emergence of various physical properties[3-5,9-11]. CoFe PBA, with chemical composition $A_xCo_y[Fe(CN)_6].nH_2O$ (A=alkali) are coordination networks with a face centered cubic (fcc) structure [4,9-11]. The cyanide (CN^-) groups bridge the Co and Fe ions in octahedral crystal fields, splitting their 3d orbitals into t_{2g} and e_g sets. This gives rise to bistable electronic/structural configurations shown in Figure 1a: $Co^{III}(S=0)Fe^{II}(S=0)$ or $Co^{II}(S=3/2)Fe^{III}(S=1/2)$. In the high spin $Co^{II}Fe^{III}$ state, the population of the antibonding Co(e_g) orbitals expands the Co-N bonds by ≈0.2 Å in comparison to the low spin Co^{III} state. This spin transition (ST) on Co is the main structural reaction coordinate Q_R, responsible for lattice expansion.

The original report of Fe-to-Co photoinduced CT by Sato *et al.* [3], forming a $Co^{II}(S=3/2)Fe^{III}(S=1/2)$ state with magnetic order at low temperature from the diamagnetic $Co^{III}(S=0)Fe^{II}(S=0)$ state, motivated many studies during the past two decades,[9,12-14] for exploring the remarkable physicochemical properties of PBA. With the long-term objective to build the next-generation devices based on functional molecules, several groups invested large efforts for developing new synthesis methods, designing molecular analogues and isolating chemically the Co-N-C-Fe switchable unit.[15,16] Similar observations in various cyanide-bridged bimetallic systems, including MnFe ferromagnets[4] or CoW molecular-bridged assemblies,[17] underlined the generalization of the photoinduced CT process.

Since the discovery of photomagnetism in PBA, the quest to understand and control the order of physical processes during the ultrafast photoreaction remained unanswered: does charge-transfer

induce spin-transition or vice versa? Very few ultrafast studies have been performed so far and their time resolution[18-20] provided a limited understanding of the CT or structural trapping dynamics. A recent theoretical work[21] discussed how the Co reaches the S = 3/2 state within ≈ 20 fs after photoexciting a low spin Co^{III} ion by an Fe-to-Co charge transfer. However, another work based on first-principles relativistic many-electron calculations[22] attributed the absorption band around 540 nm, used for photo-transformation, not to the CT $Fe^{II}t_{2g} \rightarrow Co^{III}e_g$ transitions (located at higher energy region) but to *d–d* transitions within a given metallic ion. In other words, despite the continuously growing interest in PBA, the basic ultrafast mechanism behind photophysics is still not understood, which limits the development of these broad class of materials. More than twenty years ago, Verdaguer underlined already how *"amazing are shortcomings of the oldest molecule-based inorganic system, with still many things to learn from old systems, once we look at them anew".* [23] This lack of understanding motivated our study of using emerging ultrafast X-ray-based techniques[24,25] for obtaining new insights into the photoinduced CT dynamics in a prototype CoFe PBA, by probing the evolution of charge-transfer and of the structural degrees of freedom on the femtosecond (fs) time scale. Our results reveal that the $t_{2g} \rightarrow e_g$ photoexcitation centred on the Cobalt triggers ultrafast intersystem crossing that ultimately drives the Iron to Cobalt charge transfer.

Results

We studied $Co^{III}Fe^{II}$ nanocrystals [$Cs_{0.7}Co(Fe(CN)_6)_{0.9}$], transforming under light irradiation towards the $Co^{II}Fe^{III}$ state, long-lived at low temperature[26] and rapidly relaxing above 120 K[27]. More details about the sample are given in supplementary information. X-ray Absorption Near-Edge Structure (XANES) is a relevant technique for studying photoinduced CT phenomena in PBA, because of the X-ray energy-weighted sensitivity to electronic and structural changes around the absorbing Fe and Co elements. Bleuzen et al characterized the photoinduced $Co^{III}Fe^{II}$ to $Co^{II}Fe^{III}$ transformation on very similar compounds,[28] stabilized under pressure.[13] At the Fe edge, they observed a ≈0.6 eV rigid spectral shift towards higher energy, due to the formal $Fe^{II} \rightarrow Fe^{III}$ oxidation change (see also Supplementary Fig. 6).

At the Co edge, the opposite spectral shift towards lower energy, due to the $Co^{III} \rightarrow Co^{II}$ oxidation change, occurs. In addition, the spin transition on the Co, which increases the Co-N distance due to the occupancy of antibonding e_g orbitals, shifts the first EXAFS feature around 7770 eV towards lower energy in agreement with Natoli's rule.

For monitoring the photoinduced dynamics in real-time, we used the optical pump / XANES probe technique with a time resolution $\sigma_X \approx 25$ fs RMS (IRF_{FWHM}= 58 fs) at the XPP instrument of the LCLS X-ray free-electron laser [25,29,30]. We acquired measurements from an optimized free-flowing jet of CoFe nanocrystals in aqueous solution, excited by 540 nm optical pulses and probed by X-ray pulses. Details on the experimental setups are given in the Methods section. Figures 1b and 1c show the transient intensity changes of XANES, ΔI(3ps), recorded 3 ps after photo-excitation of the ground $Co^{III}Fe^{II}$ state. The simultaneous absorption increase below and decrease above the Co K-edge (7727 eV), and the opposite changes at the Fe K-edge (7131 eV), are characteristic of the spectral shifts previously reported,[13,27] which constitute a direct proof that the Fe-to-Co CT already occurred 3 ps after photoexcitation. Since there is almost no structural reorganization near the Fe, the XANES change at the Fe edge is only due to CT (Supplementary Fig. 6) and corresponds to a 0.6 eV rigid spectral shift,[13] mainly characterized by an increase of absorption above 7131 eV and a decrease of absorption below. At the Co edge, the photoinduced spectral change we observe is in very nice agreement with that reported by Cafun[13] for the photoinduced $[Co^{III}(S=0)Fe^{II}(S=0)]$ to $[Co^{II}(S=3/2))Fe^{III}(S=1/2)]$ transformation (Supplementary Fig. 6c). The 2 eV spectral shift due to CT[13] contributes to XANES change below 7740 eV only. Above 7760 eV the XANES change is due to the shift of the first EXAFS feature towards lower energy due to the spin transition on the Co, which increases the Co-N distance in agreement with Natoli's rule. We observed a similar ultrafast shift of the first EXAFS feature during the photoinduced spin transition in $Fe(bpy)_3^{2+}$.[25]

For learning more about the ultrafast dynamics, we measured XANES changes after photoexcitation at X-ray energies, indicated by coloured lines in Figures 1b and 1c, where spectral changes after 3 ps

are strong, to increase the signal/noise ratio, or almost zero, to track intermediate states. The time-resolved data around Co (Figure 2a) and Fe (Figure 2b) K-edges indicate that the transformation occurs within a few 100s fs, with opposite absorption changes above and below both edges and opposite changes between the Fe and Co, characterizing the intermetallic CT. The dynamics do not correspond to simple exponential laws and weak damped oscillation components appear (Supplementary Fig. 8 & 9). The transient absorptions at 7727.1 eV and 7131 eV, corresponding to isosbestic points at Co and Fe edges between $Co^{III}Fe^{II}$ and photoinduced $Co^{II}Fe^{III}$ states, highlight the presence of an intermediate state (or several)s decaying within 200 fs. We performed a complementary optical pump-probe study at the Institut de Physique de Rennes, with time resolution $\sigma_{OD}\approx$80 fs, exciting the same nanocrystals with femtosecond pulses at 540 nm. Optical density changes (ΔOD, Figure 2c) for different probe wavelengths have been recorded with high signal to noise. The global spectral change, with bleaching of the 540 nm band and the appearance of new bands above and below, is characteristic of the $Co^{III}Fe^{II}$ to $Co^{II}Fe^{III}$ transformation, as measured at low temperature and in agreement with TD-DFT calculations (Supplementary Fig. 4 & 5). Optical data in Figure 2c reflect signals associated with a variety of processes evidenced by XANES, such as the transient state around the isosbestic point (627 nm) or the activation and damping of coherent oscillations with 1.65 THz frequency, more easily observed in OD change compared to XANES data, due to the higher signal/noise ratio (Supplementary Fig. 8 & 9).

Discussion

Considering the similar features in the XANES ΔI and ΔOD transients, we fit these globally with a phenomenological model including a minimum number of components ((Supplementary Fig. 7-10). A fast exponential component (τ_1=50(10) fs) is necessary to describe the XANES changes at the Co K-edge, while τ_2=200(10) fs and τ_3=450(30) fs components must be used to describe slower dynamics at both Co and Fe K-edges, especially at isosbestic points. An oscillating component is included for accounting the 1.65(2) THz vibration, with ≈600 fs damping constant. This simple global model is able to reproduce the main features of the XANES data around the Co (Figure 2a) and Fe (Figure 2b) K-

edges, as well as the ΔOD data (Figure 2c). Black lines in Figure 2 correspond to the global fit of the entire dataset. The weight of each component for each signal shown in Supplementary Fig. 9 was refined and is given in Supplementary Table 1. An important result is that there is no fast component around the Fe K-edge (Supplementary Fig. 6, 8 & 9): the main component is the 200 fs timescale, which corresponds then to the CT timescale. The red Fe-K-edge trace in Fig. 2b monitors the signal close to the isosbestic point. It does not approach zero at large delay because 7131 eV does not correspond exactly to the isosbestic point. However, this time trace shown in Supplementary Fig. 8b & 9b exhibits a single dynamics (τ_2=200 fs), easily decomposed into two components: an exponential decay due to the intermediate (INT) state(s) and an exponential increase due to the formation of the $Co^{II}Fe^{III}$ state. On the contrary, away from the Co edge (such as at 7770 eV), XANES is not sensitive to the spectral shift due to CT, but only to the structural changes accompanying the ST, responsible for the shift of the first EXAFS feature, and occurring within ≈50 fs (Supplementary Figs. 6c, 8a, 9a). The weak but significant oscillating component, observed in Fe, Co or OD data corresponds to a maximum amplitude around time delay dt=0, characteristic of the displacive nature of the structural reorganization (Supplementary Fig. 10), as it is the case during LIESST [25,31]. Supplementary Fig. 9 shows the different components in signals and underlines the fast 50 fs dynamics at the Co edge and the main 200 fs dynamics at the Fe edge.

In order to provide further support to the assignment of the optical transitions, we carried out time-dependent DFT computations[32] on a monomeric $(CN^-)_5$-Fe-C-N-Co-$(NC^-)_5$ cluster (see Figures 3b and Supplementary Fig. 5), as also performed by Johansson on VCr PBA.[20] The results indicate that the transitions in the 530-580 nm range correspond to Co^{III} d-d transitions, with a hole mainly of Co(t_{2g})-like nature and a particle mainly of Co(e_g)-like nature with some weight on the CN groups, but it does not involve the Fe centre. The transitions around 390 nm correspond to intermetallic CT from Fe to Co sites. Both the d-d nature of transitions around 540 nm and the CT nature of transitions at higher energy agree with more complex first-principles relativistic many-electron calculations for crystals.[22]

These calculations and our TD-DFT analysis, both performed in a regular lattice, do not take into account the effect of phonons, which break the symmetry and enhance the transitions. In addition, DFT calculations reveal vibration modes around 1.62 THz, corresponding to a global torsion of the network, CoN_6 and FeC_6 cores and Fe-C-N-Co bridge (videos 1-4). Such torsion modes also correspond to the mode measured around 1.5 THz by Ohkoshi on similar Mn-N-C-Fe PBA and also identified as a torsion mode of the lattice.[33]

Both theoretical calculations and experimental results indicate that the very first step involves changes around the Co site only (see also Supplementary Figs. 5 & 7) and the process thus resembles to the light-induced excited spin-state trapping process (LIESST) in isoelectronic Fe^{II} systems. The fast intermediate spin transition process on the Co can be described as involving the photoexcited Co^{III*}(S=0)Fe^{II}(S=0), the Co^{III}(S=1)Fe^{II}(S=0) state possibly, and the Co^{III}(S=2)Fe^{II}(S=0) states. We characterized these states by DFT calculations for both the monomeric $(CN^-)_5$-Co-N-C-Fe-$(CN^-)_5$ and for the Co-$(NC^-)_6$ clusters (Supplementary Fig. 2-3). The ST on the Co is responsible for the elongation of the Co-N bond and the fast changes around the Co edge. In addition to the main electronic states shown in Fig. 3, additional electronic states may be involved. However, it was shown that during LIESST these intermediate states act as mediators and that it is difficult to disentangle electronic and structural degrees of freedom.[25,31] The photoexcitation of the Co^{III}(S=0) generates an excited Co^{III*}(S=0) state that may decay in the Co^{III*}(S=1) state. For both Co^{III*} states, the population of the Co antibonding e_g states drives the Co-N bond expansion (breathing mode) which reduces the t_{2g}-e_g gap and drives the spin transition towards Co^{III}(S=2). This initial bond elongation due to spin transition on the Co occurs within ≃50 fs, which is consistent with the ½ period of the breathing mode of the Co-N_6 octahedron found by DFT (video 5). Both the timescale and the nature of the process of this spin transition are similar to the light-induced excited spin state trapping process (LIESST), reported for Fe^{II} spin-crossover molecules under d-d excitation.[34]

This bond elongation due to spin transition occurs within 50 fs and drives charge transfer (Supplementary Fig. 2-3), as shown by theoretical calculations.[35] This CT towards the $Co^{III}(S=3/2)Fe^{II}(S=1/2)$ state is responsible for the consecutive elongation of the Co-N bond monitored at 7770 eV and equilibrating within 450 fs. The formation and decay of the intermediate(s), involving changes around the CN groups (Supplementary 2, 3 & 5), contribute to the fast signal change (within the time resolution) and decay (200 fs) around the isosbestic point at the Fe edge (7129, 7131 and 7134 eV). On the contrary, there is no fast component for the other probe energies, especially at the Fe pre-edge, sensitive to the population of the Fe t_{2g} or e_g states and which monitors independently the CT dynamics within 200 fs.

Another possible mechanism could be the simultaneous CT and ST from the excited $Co^{III}(t_{2g}^5e_g^1)$-$Fe^{II}(t_{2g}^6e_g^0)$ state (green in Fig. 3) towards the $Co^{II}(t_{2g}^5e_g^2)$-$Fe^{III}(t_{2g}^5e_g^0)$ state (red). The experimental data make it possible to exclude such a process, requiring spectral shifts (associated with CT) preceding or simultaneous to EXAFS shift at 7770 eV (associated with spin transition) inconsistent with our observations. In addition, a CT from Fe t_{2g} to Co e_g orbital is not expected to be fast due to the different symmetry of the orbitals. Finally, initial MLCT states involving Co^{IV} or Fe^{III} states can also be excluded since there is no XANES signature related to the expected instantaneous spectral shift, as characterized during LIESST in $Fe(bpy)_3^{2+}$ by transient peaks at different probing energies [25].

Our experimental results, thus provide direct insight into the photoinduced electronic and structural dynamics, with an overall picture of the photoinduced process schematically represented in Figure 3. The schematic representation of the potential energy curves is based on our DFT calculations (Supplementary Fig. 2, 3 & 5) providing equilibrium Co-N bonds and t_{2g}-Co(e_g) gap. The ST, tracked through the Co-N bond elongation, occurs within ≈50 fs and is accompanied by coherent structural oscillations. Indeed, the crystalline network has no time to expand on this timescale and a torsion of the lattice is needed to accommodate the ST, as schematically shown in Figure 3c. This structural reorganization activates in a displacive way the 1.65 THz lattice torsion mode, which break local

octahedral symmetry and modulates optical and X-ray absorptions. This oscillation is damped within ≈ 600 fs by the energy transfer towards others degrees of freedom as well as by the relaxation towards a more regular structure, as lattice expansion starts to accommodate the local volume change around the Co site. However, after 3 ps some local torsions should remain within the crystal lattice, as the expansion timescale required to accommodate the Co-N bond elongation is limited to ≃6 ps, given by the ratio between the sample size (11 nm) and the speed of sound (≃2000 m/s) at which elastic deformation waves propagate. It is therefore likely that the crystal structure is not fully equilibrated after 3 ps, which may explain why the Fe XANES change is not exactly a spectral shift (Supplementary Fig. 6d).

The element-specific XANES data, sensitive to the oxidation state or structural reorganization, also allows for monitoring at the Fe K-edge the CT dynamics within ≈200 fs, as only CT contributes to spectral shift. This CT is fast because the t_{2g} symmetry of both Fe to Co orbitals allows for an efficient coupling between the Co^{III}(S=2)Fe^{II}(S=0) and the Co^{II}(S=3/2)Fe^{III}(S=1/2) states. However, CT occurs only in a second step, well after the ST. It was shown by Kawamoto[35] that the Co-N bond expansion stabilizes the $Co^{II}Fe^{III}$ state, as it decreases the t_{2g}-Co(e_g) energy gap. Our DFT calculations (Supplementary Figs. 2 & 3) give similar results: the average Co-N bond expands from 1.99 Å in the Co^{III}(S=0) state, 2.04 Å in the Co^{III}(S=1) state, to 2.06 Å in the Co^{III}(S=2) state due to the ST on the Co, which decreases the t_{2g}->Co(e_g) gap from ≃2.0 to ≃1.2 eV (Fig. 3). Since the Co-N elongation due to ST is found to take place before the CT, we conclude that it is the ultrafast ST on the Co site that drives the CT process.

Conclusions

By leveraging element-specific probing offered by hard X-ray together with high time resolution provided by the femtosecond pulse duration at X-ray Free Electron Lasers, the photoinduced electronic and structural dynamics around the metallic centres can be addressed to obtain novel understanding. The results shown in this article provide clear answer to a question debated for

decades, by demonstrating that in the photoexcited prototype CoFe PBA, the spin-transition on the Co occurs first and that the associated structural reorganizations drive the charge-transfer in a second step. Our study shows the large potential of ultra-fast X-ray science for monitoring and disentangling structural and electronic dynamics, which is of prime interest for the fundamental understanding of a multitude of CT-based phenomena in chemistry, biology or physics and more especially in the expanding family of photomagnetic materials with CT-based functions.

References

1 McCusker, J. K. Electronic structure in the transition metal block and its implications for light harvesting. *Science* **363**, 484-488 (2019).

2 Canton, S. E. *et al.* Visualizing the non-equilibrium dynamics of photoinduced intramolecular electron transfer with femtosecond X-ray pulses. *Nature Communications* **6**, 6359 (2015).

3 Sato, O., Iyoda, T., Fujishima, A. & Hashimoto, K. Photoinduced Magnetization of a Cobalt-Iron Cyanide. *Science* **272**, 704-705 (1996).

4 Ohkoshi, S. & Tokoro, H. Photomagnetism in Cyano-Bridged Bimetal Assemblies. *Accounts of Chemical Research* **45**, 1749-1758 (2012).

5 Ferlay, S., Mallah, T., Ouahes, R., Veillet, P. & Verdaguer, M. A Room-Temperature Organometallic Magnet Based on Prussian Blue. *Nature* **378**, 701-703 (1995).

6 Liedy, F. *et al.* Vibrational coherences in manganese single-molecule magnets after ultrafast photoexcitation. *Nature Chemistry*, doi:10.1038/s41557-020-0431-6 (2020).

7 Collet, E. *et al.* Laser-induced ferroelectric structural order in an organic charge-transfer crystal. *Science* **300**, 612-615 (2003).

8 Chollet, M. *et al.* Gigantic Photoresponse in ¼-Filled-Band Organic Salt (EDO-TTF)2PF6. *Science* **307**, 86-89 (2005).

9 Cartier dit Moulin, C. *et al.* Photoinduced Ferrimagnetic Systems in Prussian Blue Analogues CIxCo4[Fe(CN)6]y (CI = Alkali Cation). 2. X-ray Absorption Spectroscopy of the Metastable State. *Journal of the American Chemical Society* **122**, 6653-6658 (2000).

10 Risset, O. N. *et al.* Light-Induced Changes in Magnetism in a Coordination Polymer Heterostructure Rb0.24Co[Fe(CN)6]0.74@K0.10Co[Cr(CN)6]0.70·nH2O and the Role of the Shell Thickness on the Properties of Both Core and Shell. *Journal of the American Chemical Society* **136**, 15660-15669 (2014).

11 Aguila, D., Prado, Y., Koumousi, E. S., Mathoniere, C. & Clerac, R. Switchable Fe/Co Prussian blue networks and molecular analogues. *Chemical Society Reviews* **45**, 203-224 (2016).

12 Shimamoto, N., Ohkoshi, S., Sato, O. & Hashimoto, K. Control of Charge-Transfer-Induced Spin Transition Temperature on Cobalt−Iron Prussian Blue Analogues. *Inorganic Chemistry* **41**, 678-684 (2002).

13 Cafun, J. D. *et al.* Room-temperature photoinduced electron transfer in a Prussian blue analogue under hydrostatic pressure. *Angew Chem Int Ed Engl* **51**, 9146-9148 (2012).

14 Verdaguer, M. *et al.* Molecules to build solids: high TC molecule-based magnets by design and recent revival of cyano complexes chemistry. *Coordination Chemistry Reviews* **190–192**, 1023-1047 (1999).

15 Koumousi, E. S. *et al.* Metal-to-Metal Electron Transfer in Co/Fe Prussian Blue Molecular Analogues: The Ultimate Miniaturization. *Journal of the American Chemical Society* **136**, 15461-15464 (2014).

16 Mercurol, J. *et al.* [FeIILSCoIIILS]2 [Leftrightarrow] [FeIIILSCoIIHS]2 photoinduced conversion in a cyanide-bridged heterobimetallic molecular square. *Chem Commun* **46**, 8995-8997 (2010).

17 Miyamoto, Y. *et al.* Photo-induced magnetization and first-principles calculations of a two-dimensional cyanide-bridged Co-W bimetal assembly. *Dalton Trans* **45**, 19249-19256 (2016).

18 Asahara, A. *et al.* Ultrafast dynamics of reversible photoinduced phase transitions in rubidium manganese hexacyanoferrate investigated by midinfrared CN vibration spectroscopy. *Physical Review B* **86** (2012).
19 Moritomo, Y. *et al.* Photoinduced Phase Transition into a Hidden Phase in Cobalt Hexacyanoferrate as Investigated by Time-Resolved X-ray Absorption Fine Structure. *Journal of the Physical Society of Japan* **82**, 033601 (2013).
20 Johansson, J. O. *et al.* Directly probing spin dynamics in a molecular magnet with femtosecond time-resolution. *Chem Sci* **7**, 7061-7067 (2016).
21 van Veenendaal, M. Ultrafast intersystem crossings in Fe-Co Prussian blue analogues. *Sci Rep* **7**, 6672 (2017).
22 Watanabe, S. *et al.* Intra- and inter-atomic optical transitions of Fe, Co, and Ni ferrocyanides studied using first-principles many-electron calculations. *Journal of Applied Physics* **119**, 235102 (2016).
23 Verdaguer, M. Molecular Electronics Emerges from Molecular Magnetism. *Science* **272**, 698-699 (1996).
24 Chergui, M. & Collet, E. Photoinduced structural dynamics of molecular systems mapped by time-resolved x-ray methods. *Chemical Reviews* **117**, 11025–11065 (2017).
25 Lemke, H. T. *et al.* Coherent structural trapping through wave packet dispersion during photoinduced spin state switching. *Nat. Commun.* **8**, 15342 (2017).
26 Trinh, L. *et al.* Photoswitchable 11 nm CsCoFe Prussian Blue Analogue Nanocrystals with High Relaxation Temperature. *Inorganic Chemistry* **59**, 13153-13161, doi:10.1021/acs.inorgchem.0c01432 (2020).
27 Zerdane, S. *et al.* Probing Transient Photoinduced Charge Transfer in Prussian Blue Analogues with Time-Resolved XANES and Optical Spectroscopy. *Eur J Inorg Chem* **2018**, 272-277 (2018).
28 Bordage, A. & Bleuzen, A. Influence of the number of alkali cation on the photo-induced CoIIIFeII↔CoIIFeIII charge transfer in Csx CoFe PBAs – A Co K-edge XANES study. *Radiat Phys Chem* **175**, 108143 (2020).
29 Chollet, M. *et al.* The X-ray Pump-Probe instrument at the Linac Coherent Light Source. *Journal of Synchrotron Radiation* **22**, 503-507 (2015).
30 Harmand, M. *et al.* Achieving few-femtosecond time-sorting at hard X-ray free-electron lasers. *Nature Photonics* **7**, 215-218 (2013).
31 Zerdane, S. *et al.* Comparison of structural dynamics and coherence of d–d and MLCT light-induced spin state trapping. *Chem. Sci.* **8**, 4978-4986, doi:10.1039/c6sc05624e (2017).
32 Frisch, M. J. e. a. *Gaussian, Inc., Wallingford CT* (2016).
33 Ohkoshi, S. I. *et al.* Cesium ion detection by terahertz light. *Sci Rep* **7**, 8088 (2017).
34 Zerdane, S., Cammarata, M., Iasco, O., Boillot, M. L. & Collet, E. Photoselective MLCT to d-d pathways for light-induced excited spin state trapping. *The Journal of chemical physics* **151**, 171101 (2019).
35 Kawamoto, T. & Abe, S. Mechanism of reversible photo-induced magnetization in prussian blue analogues. *Phase Transitions* **74**, 209-233 (2006).

Acknowledgements

Funding: E.C and M.C. acknowledge the support of Rennes Métropole, ANR (ANR-13-BS04-0002 FEMTOMAT and ANR-15-CE32-0004 Bio-XFEL), Centre National de la Recherche Scientifique (CNRS, PEPS SASLELX), Fonds Européen de Développement Régional (FEDER) and Région Bretagne (ARED 8925/XFELMAT). M.C., L.B., M.L., C.E., M.T acknowledge the support of European Union Horizon2020

under the Marie Sklodowska-Curie Project “X-Probe” Grant No. 637295. The authors would like to thank A. Bleuzen for sharing published XANES data used in Supplementary Fig. 7. Use of the Linac Coherent Light Source (LCLS), SLAC National Accelerator Laboratory, is supported by the U.S. Department of Energy, Office of Science, Office of Basic Energy Sciences under Contract No. DE-AC02-76SF00515.

Author Contributions

E.C. and M.Ca. conceived the project. S.M., L.C. and T.M. synthesized and characterized the CoFe sample. M.Ca., S.Z., L.B., G.A., C.E., M.T., M.L., J.R.A.M., M.G., D.Z. and E.C. performed the femtosecond XAS experiment. S.Z. and G.A. performed the optical study. S.Z., M.Ca and E.C. analyzed the data. S.F.M. performed the DFT and TD-DFT calculations. E.C. and M.Ca set the physical picture for interpreting the data. E.C. and M.Ca wrote the paper. All authors contributed to discussions and gave comments on the manuscript.

Competing interests: Authors declare no competing interests.

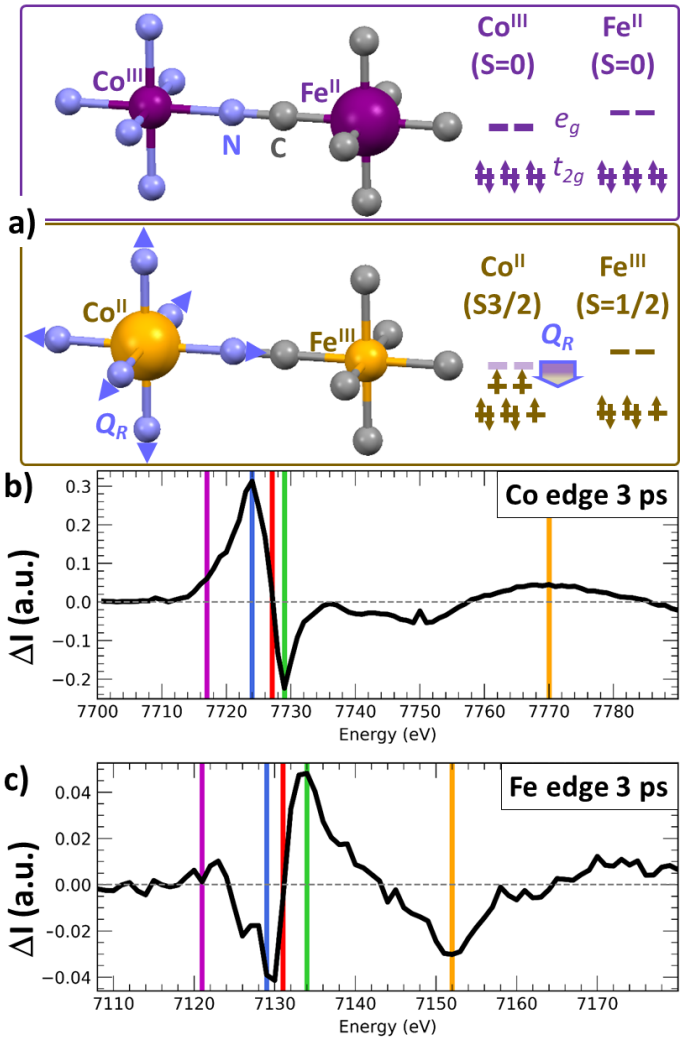

Figure 1 | CoFe PBA and X-ray absorption fingerprints of the transformation. (**a**) The cyanide-bridged coordination network with a schematic representation of the Co^{III}(S=0)Fe^{II}(S=0) and Co^{II}(S=3/2)Fe^{III}(S=1/2) states, where the charge transfer is accompanied by a spin transition on the Co. The bleu arrows indicate that upon filling up of the e_g orbitals the Co-N distance increases (***Q_R*** mode), which closes the Fe(t_{2g})-Co(e_g) gap as indicated by the coloured arrow. (**b,c**) XANES spectral changes observed at the Co and Fe K-edges 3 ps after photoexcitation at 540 nm of CoFe nanocrystals and measured using femtosecond X-ray pulses at LCLS free-electron laser. The coloured lines of panels b and c indicate X-ray energies for which high time resolution data have been measured. The data shown in figure 2a and 2b use the same colour code.

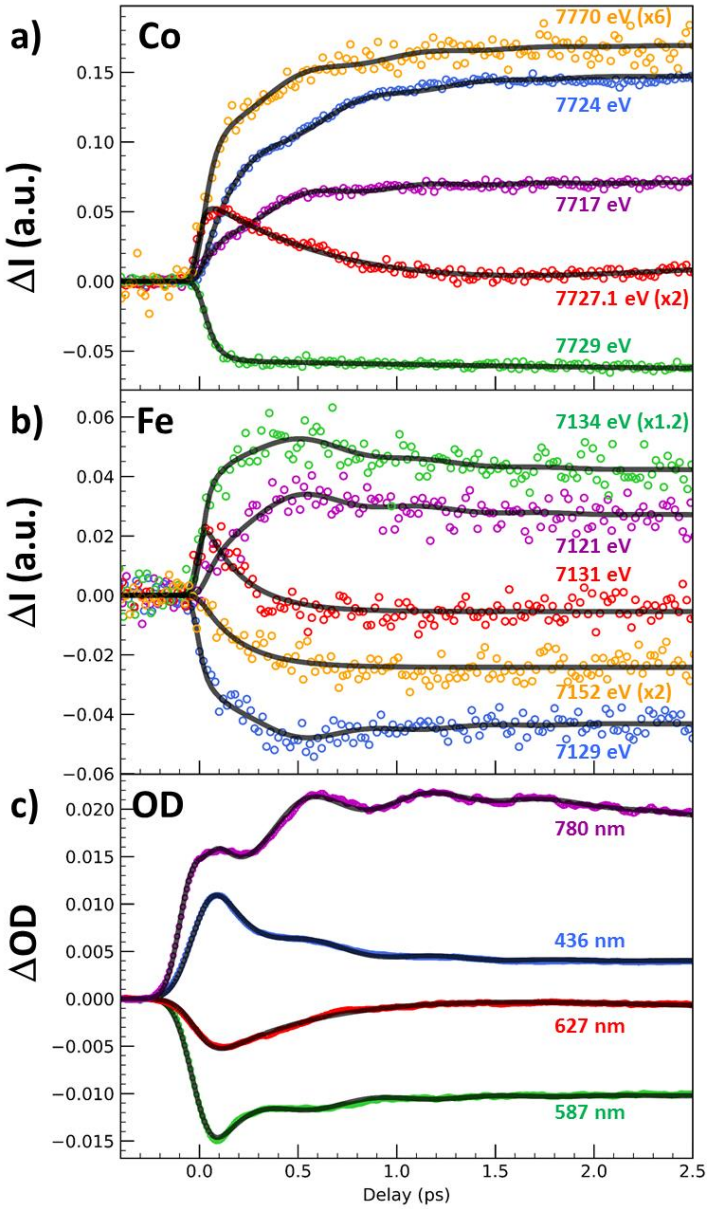

Figure 2 | Disentangling spin transition and charge-transfer dynamics in real-time. (**A**) Time scans after photoexcitation at 540 nm of the X-ray absorption intensity change (ΔI) at selected energies around the Co **(a)** and around the Fe K-edges **(b)** and of the optical density change (ΔOD) at different probing wavelengths **(c)**. The data reveal a 50 fs component attributed to ST (mainly at Co edge), a 200 fs component attributed to CT (seen at both the Fe and Co K-edges), a 450 fs component attributed to vibrational cooling and a coherent oscillation (at 1.65 THz) damped with a 600 fs timescale. Black lines correspond to the global fit of the entire dataset with the same physical parameters and time constant mentioned above and only the amplitudes of each component have been refined (Supplementary Table 1). Colour code of panels (**a**) and (**b**) matches the figures 1b and 1c.

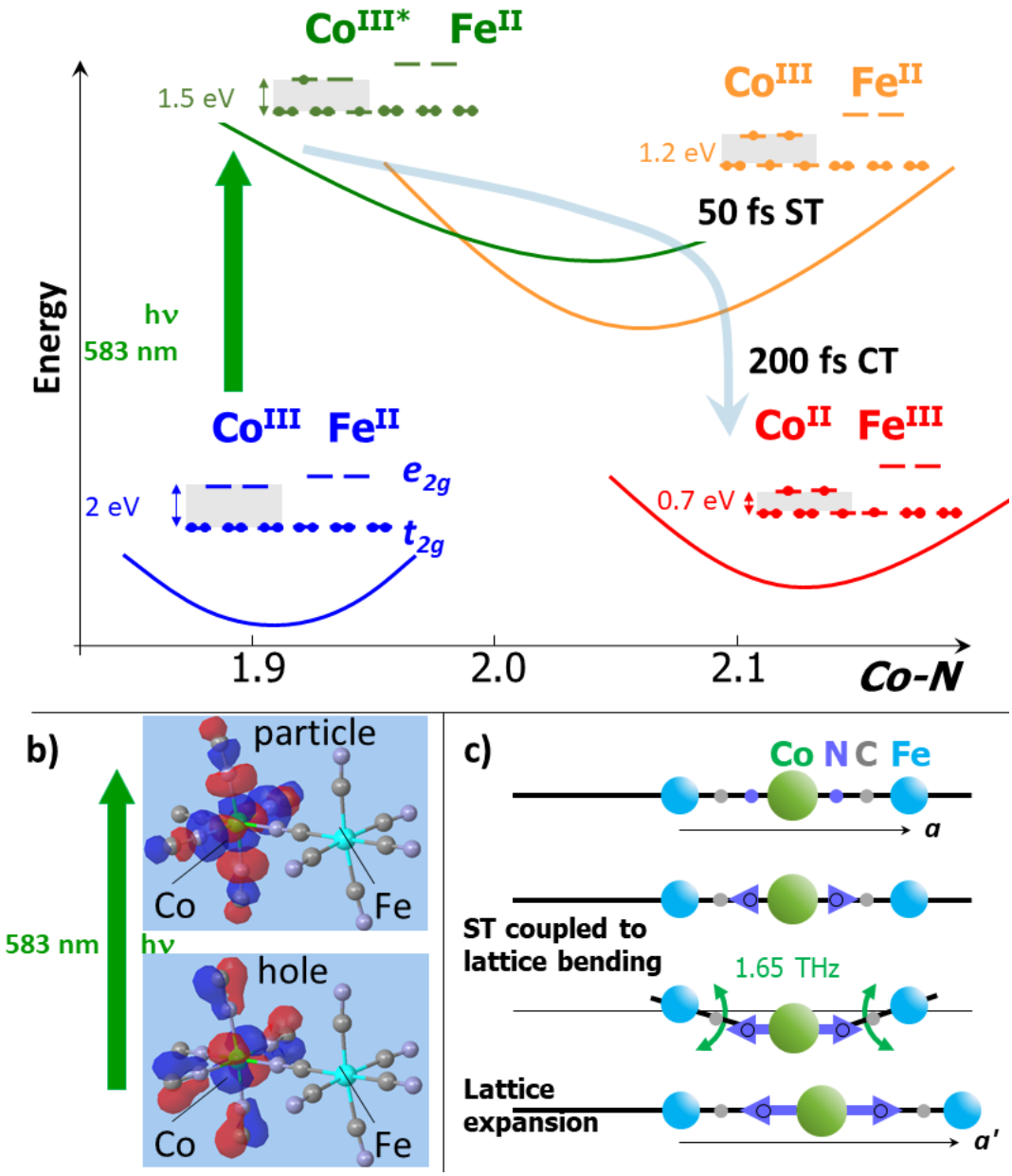

Figure 3 | Spin-transition inducing charge-transfer. (a) Schematic representation of the PES of different key states involved in the process. The optical excitation of the ground $Co^{III}Fe^{II}$ state (blue) leads to an electronically excited $Co^{III*}Fe^{II}$ state (green) by promoting one electron from the Co(t_{2g}) to the Co(e_g) orbital, as obtained from TD-DFT calculations **(b)**. The population of the antibonding e_g orbitals elongates Co-N bonds, driving so the spin transition (ST) within 50 fs on the Co towards the Co^{III}(S=2)Fe^{II}(S=0) state (orange), which closes the Fe^{II}(t_{2g}) - Co^{III}(e_g) gap (grey background). The consecutive CT results from the electronic decay within 200 fs between the Fe(t_{2g}) to the Co(t_{2g}) orbitals, leading to the Co^{II}(S=3/2)Fe^{III}(S=1/2) state. **(c)** As the Co-N bonds elongate during the ST, the lattice has to distort to accommodate the local structural change, activating so the lattice torsion mode at 1.65 THz, which is damped by the following expansion of the lattice parameter from **a** to **a'**.

Methods

CoFe nanoparticles

We used a colloidal solution of CsCoFe Prussian blue analogue nanoparticles (11±1.5 nm) of formula $[Cs_{0.7}Co(Fe(CN)_6)_{0.9}]^{n-}$, mainly made of active and vacancy-free $CsCo^{III}Fe^{II}$ species, and recovered as a solid sample by cethyltrimethyl ammonium (CTA^+) (supplementary information). Our previous XANES study with 100 ps time resolution [27] has shown that these particles are stables in water and that the lifetime of the photoinduced $Co^{II}Fe^{III}$ state is shorter than 1 ms at room temperature. The particles were fully characterized in ref[26].

Femtosecond optical pump / XANES probe.

The time resolved X-ray absorption signal of CoFe nanoparticles was measured using the pump/probe technique through total fluorescence, by using the same method as presented in ref [25]. We used a silicon (111) double crystal monochromator available at the X-ray Pump Probe instrument of the LCLS. CoFe nanocrystals dispersed in water circulated via a closed loop system through a 30 µm diameter liquid Rayleigh jet, to mitigate any laser or X-ray induced damage. The sample was excited by 540 nm pulses from a Ti:sapphire laser system and an Optical Parametric Amplifier (OPerA Solo, Coherent). The relative X-ray to optical pulses arrival time was recorded using the timing tool diagnostic [30]. The X-ray beam was focused by two appropriate sets of Be lenses (one for each K-edge). The chromatic effects of the lenses are negligible over the tens of eV scan range for the moderate chosen focal spot size of 10-20 µm. The ~30 eV wide radiation central wavelength produced by the machine was adjusted using the so-called "Vernier" to be synchronized with the monochromator. The pump laser was focus to 140 x 220 μm^2. The excitation energy was set to 25 µJ resulting in fluence of 0.8 mJ/mm^2, below the observed onset of nonlinear signal response at 1.5mJ/mm^2. The overall time resolution was found to be σ_X =25 fs (58 fs FWHM) during the fit procedure (Supplementary Fig. 7).

Femtosecond optical pump / optical probe spectroscopy.

We used an optical pump-probe method to probe the photoinduced dynamics in CoFe nanocrystals dispersed in solution. We set the wavelength of the pump laser pulse to 540 nm and we measured the time-resolved optical density (OD) change at various probing wavelengths. We configured the femtosecond optical pump-probe experiments in transmission geometry with a quasi-collinear configuration of pump and probe beams, which allowed reaching a time resolution of 80 fs RMS. We performed pump-probe measurements in a stroboscopic way by pumping the sample with at 500 Hz repetition rate and probing the OD change at 1 kHz.

DFT and TD-DFT calculations.

For understanding the optical spectral changes and the transitions involved in the process, we used time-dependent DFT (TD-DFT) computations for $(CN^{-})_5$-Fe-C-N-Co-$(NC^{-})_5$ cluster and $Co(NC)_6$ clusters. We performed calculations in both $Co^{III}(S=0)Fe^{II}(S=0)$ or $Co^{II}(S=3/2)Fe^{III}(S=1/2)$ states, starting from geometry optimized molecule with UB3LYP/6-31g(d,p) functional-basis set (i.e. an unrestricted hybrid functional accounting for paramagnetic configurations couples with an all-electron basis set preferred to limited valence one as LANL2DZ). Preliminary to these calculations, geometry optimizations followed by deriving the vibration frequencies were carried out, with Gaussian 09 code [32]. Frequencies are determined from the second derivatives of the energy with respect to the atomic positions and then operating transformation to mass-weighted coordinates. TD-DFT, as implemented in the Gaussian 09 code, package was applied for calculating oscillator strength and obtaining the "natural transition orbitals" (NTO) through an account for hole–particle pairs, which are then used to interpret the initial photo-excitation process. In order to account for the spin transition on the Co, while keeping Fe in S=0, and the CT processes, both stabilized by molecular deformations around the Co, we model the $Co(NC)_6$ cluster with specific oxidation states. Divalent and trivalent Cobalt hexacyanide charged molecules were modeled based on a starting octahedral environment with central cobalt surrounded

by 6 $(NC)^{-}$. The quantum chemical calculations were carried out similarly to dinuclear PBA FeCo using G09 program (license University of Bordeaux) with restricted B3LYP hybrid functional for S=0 state and UB3LYP unrestricted hybrid functional for all other configurations; the choice of the basis set was 3-21g; tests with higher basis sets as 6-31g did not change the results. After full geometry optimizations, the 6 Co-N bonds are equivalent for the state Co^{3+}(S=0) in O_h field, while for the other states different Co-N distances were identified in relation with the splitting of the orbitals in the D_{4h} field. Results are presented in supplementary information.

Data availability

The datasets generated and analysed during the current study are available in the HAL repository,

Supplementary Information

Charge-transfer driven by ultrafast spin-transition in a CoFe Prussian blue analogue

Marco Cammarata[1,*] Serhane Zerdane[1], Lodovico Balducci[1], Giovanni Azzolina[1], Sandra Mazerat[2], Cecile Exertier[3], Matilde Trabuco[3], Matteo Levantino[4], Roberto Alonso-Mori[5], James M. Glownia[5], Sanghoon Song[5], Laure Catala[2], Talal Mallah[2] , Samir F. Matar[6,7], Eric Collet[1*]

*Correspondence to: eric.collet@univ-rennes1.fr and marco.cammarata@univ-rennes1.fr

[1]Univ Rennes, CNRS, IPR (Institut de Physique de Rennes) - UMR 6251, F-35000 Rennes, France.

[2] Institut de Chimie Moléculaire et des Matériaux d'Orsay, Université Paris-Sud, CNRS, Université Paris-Saclay, 91405 Orsay cedex, France.

[3] Department of Biochemical Sciences «A.R. Fanelli», Sapienza University of Rome, P.le A. Moro 5, 00185 Rome, Italy

[4] ESRF - The European Synchrotron, 71 Avenue des Martyrs, 38000 Grenoble, France

[5]Linac Coherent Light Source, SLAC National Accelerator Laboratory, Menlo Park, CA-94025, USA.

[6] ICMCB, CNRS UMR 5026, Université de Bordeaux, F-33600 Pessac, France.

[7]Lebanese German University (LGU), Sahel Alma Campus, PO Box 206, Jounieh, Lebanon

List of Supplementary Materials:

Video 1-4 Torsion modes.

Video 5 breathing mode.

Fig. 1. Size of the nanoparticles and X-ray diffraction pattern.

Fig. 2. DFT for the $(CN)_5$-Co-N-C-Fe-$(CN)_5$ cluster.

Fig. 3. DFT for the $Co(NC)_6$ cluster.

Fig. 4 Calculated oscillator strength (left) and measured OD change after photoexcitation at 10 K (right).

Fig. 5. Natural transition orbitals (NTO) of the $Co^{III}Fe^{II}$ state.

Fig. 6. XANES spectral changes.

Fig. 7. XANES IRF_X.

Fig. 8. Independent fits.

Table 1 and Fig. 9. Global fit of the dynamics.

Fig. 10. Oscillating component in the fit of the data.

CoFe nanoparticles

A colloidal solution of CsCoFe Prussian blue analogue nanoparticles was prepared by adding an aqueous solution of $K_3[Fe^{III}(CN)_6]$ (50 ml, 10^{-3} mol) to 50 ml of an aqueous solution containing $[Co^{II}(H_2O)_6]Cl_2$ (10^{-3} mol) and CsCl ($2x10^{-3}$ mol). The sample was characterized by various complementary techniques including transmission electron microscopy, XPS, magnetism, optical spectroscopy, X-ray diffraction and photocrystallography as well as EPR spectroscopy (ref 26). Energy Dispersive X-ray Spectroscopy (EDS) was performed on the particles recovered as a solid sample by cethyltrimethyl ammonium (CTA^+) that allows reconstructing their average formula as $[Cs_{0.7}Co(Fe(CN)_6)_{0.9}]^{n-}$. Infrared spectroscopy is consistent with the presence of a very small amount of passive $Fe^{III}Co^{II}Fe^{II}$ species assumed to be located at the nanocrystals' surface while the core is mainly made of the active and vacancy-free $CsCo^{III}Fe^{II}$. The analysis revealed a majority (≈70%) of low spin and photoactive diamagnetic $Co^{III}Fe^{II}$ pairs occupying the core of the nanocrystals and a mixture of $Co^{II}Fe^{II}$ and $Co^{II}Fe^{III}$ species (see also Fig. 7). Energy Dispersive X-ray spectroscopy allowed us to determine the following chemical formula: $(CTA)_{0.4}[Cs_{0.7}Co\{Fe(CN)_6\}_{0.9}]\bullet H_2O$. After light excitation, the change of magnetic susceptibility and lattice parameters probed by X-ray diffraction confirm the photoinduced transformation of $Co^{III}Fe^{II}$ species to the $Co^{II}Fe^{III}$ state. Our previous XANES study with 100 ps time resolution *(25)* has shown that the particles are stable in water and that the lifetime of the photoinduced $Co^{II}Fe^{III}$ state is shorter than 1 ms at room temperature, allowing to perform pump-probe studies. Dynamic light scattering of the as-obtained solution shows the presence of objects in 10-12 nm hydrodynamic size (Fig. 1a). Transmission electronic microscopy confirmed the size of the crystals to 11±1.5 nm as depicted in Fig. 1b.

The XRD pattern (Fig. 1c) of the CoFe sample shows the good crystalline quality of the nanoparticles and is characteristic of the FCC lattice. The cell parameter is a=10.03±0.05 Å, which is close to the one of the pure $CsCo^{III}Fe^{II}$ network with a=9.96 Å. This confirms that the sample is made of a majority of $Co^{III}Fe^{II}$ species and we estimate a 28% contribution from the $Co^{II}Fe^{III}$ and $Co^{II}Fe^{II}$ species, and 72% of the diamagnetic $Co^{III}Fe^{II}$ network.

Our previous XANES study with 100 ps time resolution *(27)* has shown that the particles are stables in water and that the lifetime of the photoinduced $Co^{II}Fe^{III}$ state is shorter than 1 ms at room temperature, allowing for performing pump-probe studies.

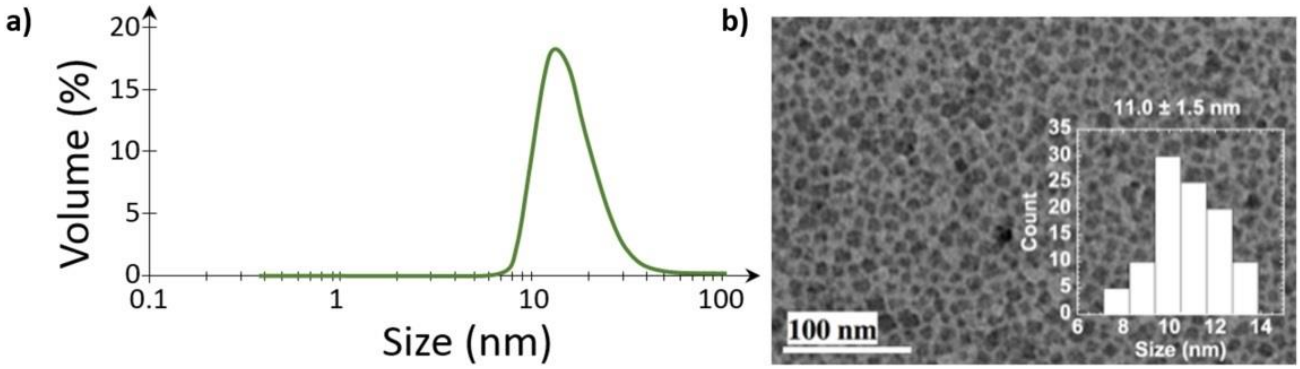

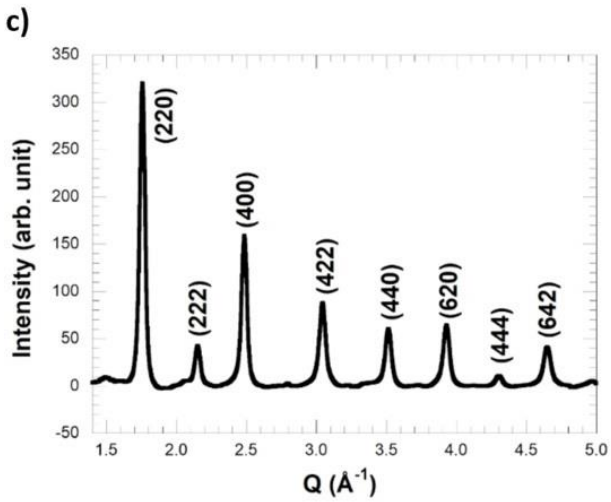

Fig. 1. Size of the nanoparticles and X-ray diffraction pattern. (a) Dynamic light scattering of the as-prepared solution of the CoFe nanocrystals. **(b)** Transmission Electron Microscopy image of CoFe nanocrystals and size distribution. **(c)** X-ray powder diffraction pattern of the $[Cs_{0.7}Co(Fe(CN)_6)_{0.9}]^{n-}$ a solid sample recovered by cethyltrimethyl ammonium (CTA^+) characteristic of the fcc lattice.

DFT and TD-DFT calculations.

We performed DFT and TDDFT calculations with Gaussian 09. The calculations go through two main steps.

The first step is to geometry optimize the molecule. Then the second step consists of calculating the force constants (k) through selective displacements of the molecule as stretching, torsion or other types of modes. There are (3N-6) modes in nonlinear molecules, N being the number of atoms. The resulting force constants k_N and the reduced mass provide the frequencies of the vibration modes. We performed such DFT calculations on a monomeric $(CN^-)_5$-Co-N-C-Fe-$(CN^-)_5$ cluster for both the $Co^{III}(S=0)Fe^{II}(S=0)$ state and the $Co^{II}(S=3/2)Fe^{III}(S=1/2)$ state (Fig. 2). The molecular geometry changes between both states with the characteristic elongation of the Co-N bonds from 1.93 Å for the $Co^{III}(S=0)Fe^{II}(S=0)$ state to 2.12 Å for the $Co^{II}(S=3/2)Fe^{III}(S=1/2)$ state. We performed a similar calculation in the Co_2Fe_2 square cluster in the LS state. All these calculations show similar torsion modes of the Co-N-C-Fe bridge at around 1.6 THz in each state.

- Video 1 & 2 show torsion modes of the $Co^{II}(S=3/2)Fe^{III}(S=1/2)$ state at 1.44and 1.62 THz
- Video 3 shows the torsion mode of the $Co^{III}(S=0)Fe^{II}(S=0)$ state at 1.85 THz
- Video 4 shows the torsion mode of the $Co_2^{III}Fe_2^{II}$ state at 1.56 THz

Such a torsion mode also corresponds to the mode measured around 1.5 THz by Ohkoshi on similar Mn-N-C-Fe PBA (ref 33) and also identified as involving a torsion of the lattice and especially the cyano bridge.

- Video 5 shows the Co-N breathing mode around 11.2 THz (90 fs period) for the $Co^{II}(S=3/2)Fe^{III}(S=1/2)$ state. The spin-transition timescale is limited by the elongation time of the Co-N bonds from the $Co^{III}(S=0)$ to $Co^{II}(S=2)$ potentials, which is of the order of the ½ period of the breathing mode of the CoN_6 octahedron, i.e. 45 fs.

We also performed time dependent DFT calculation, equally based on the DFT with the major difference of replacing the Hohenberg-Kohn first theorem by time-dependent Runge-Gross theorem introducing time–dependence. The G09 program starts from previously obtained geometry minimum ground state energy and operates vertical excitation calculations (without structural rearrangement) with single-point TD-DFT of the absorption energy: initial state, excited states, from the lowest to the highest. This will be used to identify which excited states are of interest. That's how we get the (absorption) UV-VIS spectrum and the NTO (Natural Transition Orbitals) with the "hole electron" schematics excited states transition.

In order to provide additional information, we used Gaussian to calculate different electronic states with different spin multiplicities. In addition to the ground $Co^{III}(S=0)Fe^{II}(S=0)$ state and the photoinduced state $Co^{II}(S=3/2)Fe^{II}(S=1/2)$, we calculated the excited $Co^{III}*(S=1)Fe^{II}(S=0)$ state, which has the same Co t_{2g}^5 - Co e_g^1 electronic distribution as the initially excited $Co^{III}*(S=0)Fe^{II}(S=0)$ state and therefore both $Co^{III}*$ excited states have similar structure and energy. However, the $Co^{III}*(S=0)Fe^{II}(S=0)$ state is not accessible with Gaussian as the stable state S=0 is the ground $Co^{III}(S=0)Fe^{II}(S=0)$ state. We used the same 3-21g basis set, but we had to use the gradient GGA functional PBE (J. Perdew, K. Burke, M. Ernzerhof, Phys. Rev. Lett. 77 (1996) 3865), as the B3LYP hybrid (Hartree-Fock+DFT) used for $Co^{III}(S=0)Fe^{II}(S=0)$ and $Co^{II}(S=3/2)Fe^{III}(S=1/2)$ didn't lead to converged results for $Co^{III}(S=1)Fe^{II}(S=0)$ calculations. The calculations provide valuable information (see Fig. 2) about the nature of the frontier molecular orbitals including LUMO and HOMO, the Co(t_{2g})-Co(e_g) gap and the structure (Co-N bonds). The calculation did not converge for the $Co^{III}(S=2)Fe^{II}(S=0)$ state.

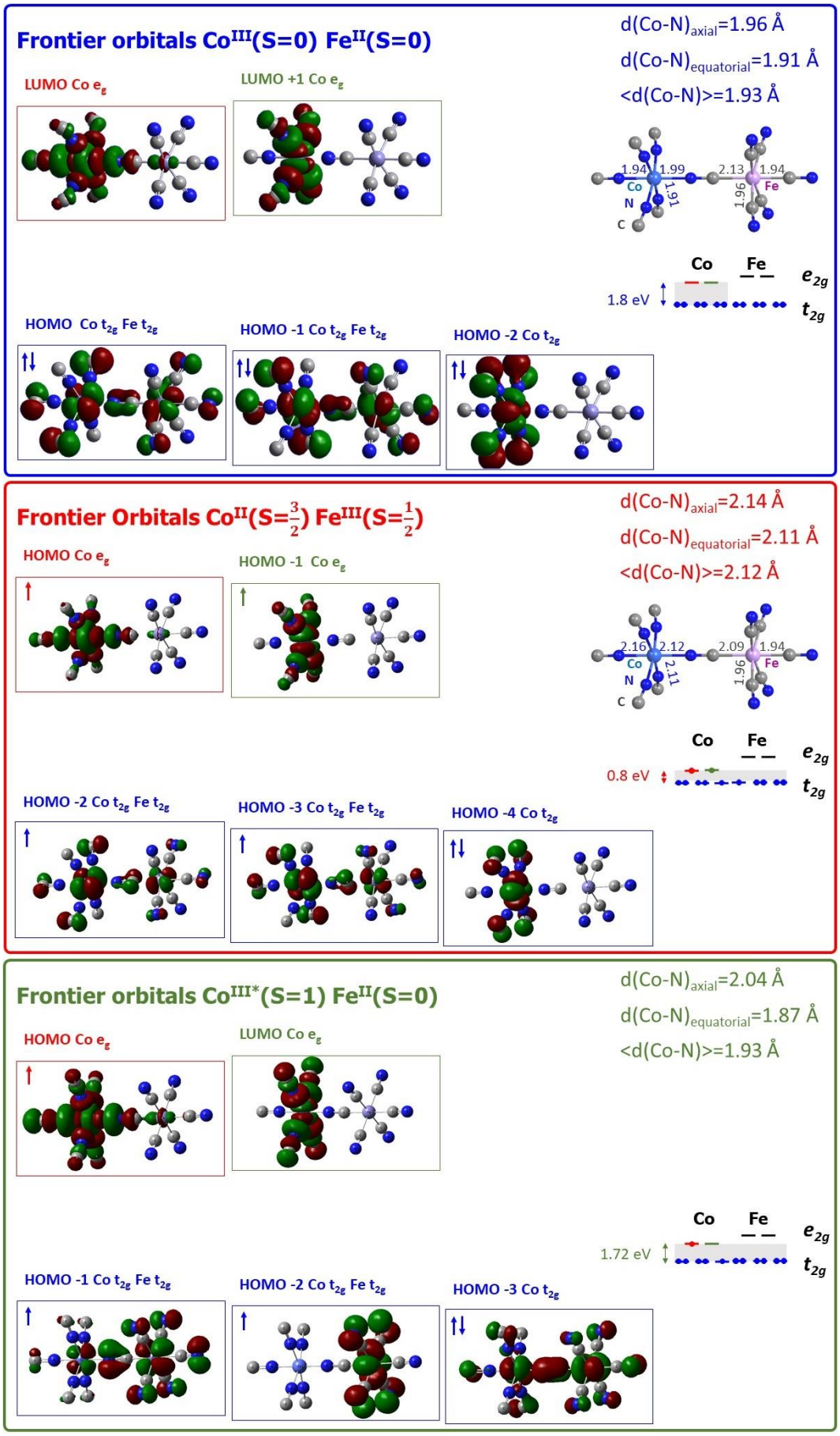

Fig. 2. DFT for the $(CN)_5$-Co-N-C-Fe-$(CN)_5$ cluster. Orbitals and t_{2g}-Co(e_g) gap for different electronic states.

In order to account for the spin transition on the Co, while keeping Fe in S=0, and the CT processes, both stabilized by molecular deformations around the Co, we modeled the $Co(NC)_6$ cluster with specific oxidation and spin states. Divalent and trivalent cobalt hexacyanide charged molecules were modeled based on a starting octahedral environment with central cobalt surrounded by 6 $(NC)^-$. The quantum chemical calculations were carried out similarly to dinuclear PBA FeCo using G09 program (license University of Bordeaux) with restricted B3LYP hybrid functional for S=0 state and UB3LYP unrestricted hybrid functional for all other configurations; the choice of the basis set was 3-21g; tests with higher basis sets as 6-31g did not change the results. After full geometry optimizations, the 6 Co-N bonds are equivalent for the state Co^{3+}(S=0) in O_h field, while for the other states different Co-N distances were identified in relation with the splitting of the orbitals in the D_{4h} field, as indicated in Fig. 3. Our calculations agree with well-known features for LIESST in isoelectronic Fe^{II} complexes undergoing spin transition: on the pathway Co^{III}(S=0) -> Co^{III}*(S=0) -> Co^{III}*(S=1) -> Co^{III}(S=2), the t_{2g}-e_g gap closes and the Co-N bonds expand. This is due to the fact that the LUMO in the Co^{III}(S=0) and HOMO in the Co^{III}*(S=0), Co^{III}*(S=1), Co^{III}(S=2) are clearly Co e_g like character. The Co-N bond expands even more in the Co^{II}(S=3/2) state.

The calculations for $(CN^-)_5$-Co-N-C-Fe-$(CN^-)_5$ and $Co(CN^-)_6$ clusters are in good agreement and in Fig. 2 we represent the different PEC with typical Co-N bond length and t_{2g}-e_g gap:

- the Co^{III}(S=2)Fe^{II}(S=0) state with Co-N ≈ 1.89 Å and t_{2g}-e_g gap ≈ 2.3 eV
- the Co^{III*}(S=1)Fe^{II}(S=0) state with axial Co-N ≈ 2.04 Å and t_{2g}-e_g gap ≈ 1.3 eV
- the Co^{III}(S=2)Fe^{II}(S=0) state, with axial Co-N ≈ 2.06 Å and t_{2g}-e_g gap ≈ 1.2 eV
- the Co^{II}(S=3/2)Fe^{II}(S=1/2) state, with axial Co-N ≈ 2.13 Å and t_{2g}-e_g gap ≈ 0.6 eV.

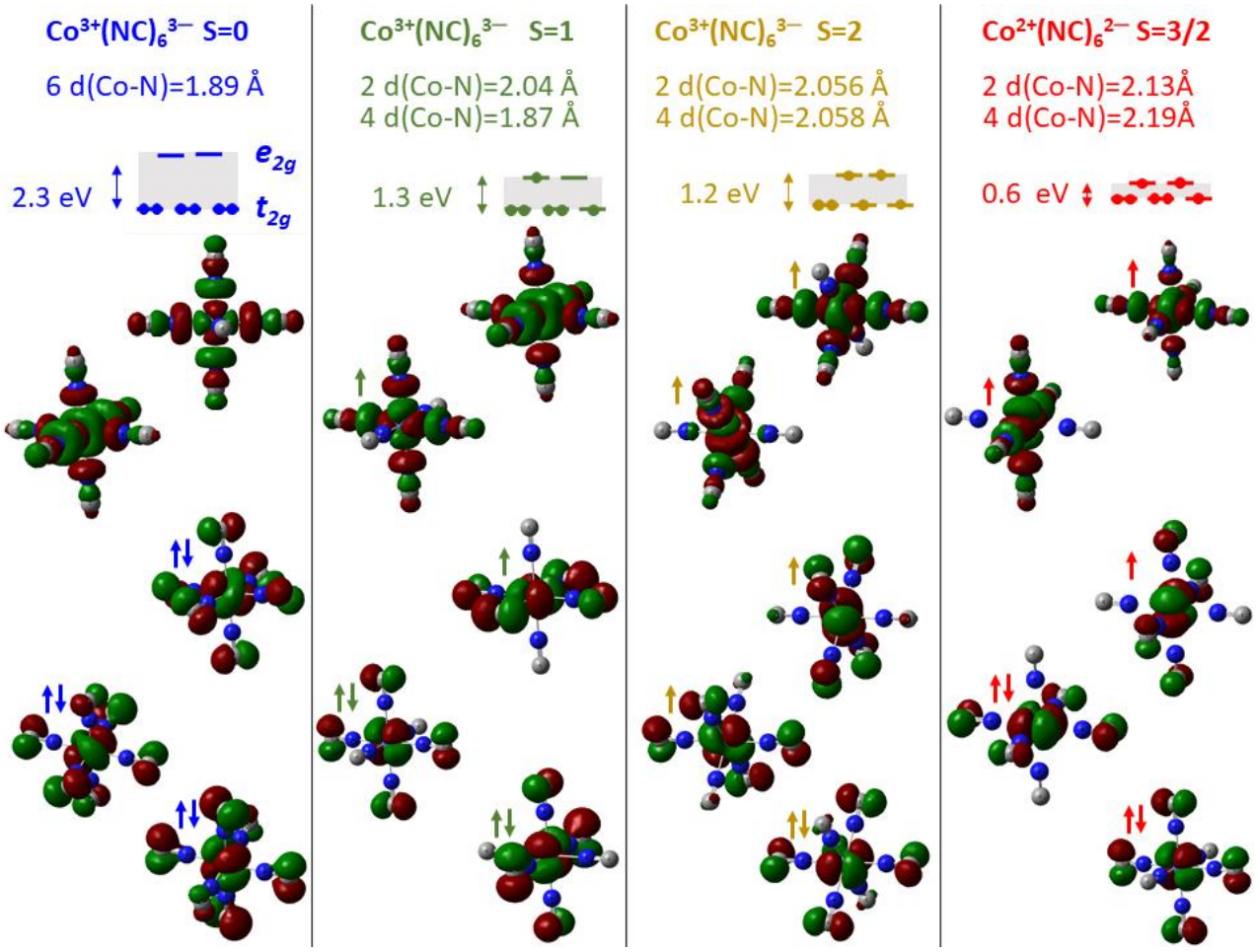

Fig. 3. DFT for the $Co(NC)_6$ cluster. Orbitals, Co-N bond length and t_{2g}-Co(e_g) gap for different electronic states.

The (Fig. 4) compares the calculated oscillator strength with the OD measurements for the ground state $Co^{III}Fe^{II}$ and the photoinduced $Co^{II}Fe^{III}$ state at 10 K. Fig. 5 shows the results of TD-DFT calculations. For the $Co^{III}Fe^{II}$ state, the band in the 530-580 nm range corresponds to Co d-d transitions: the hole has mainly a Co(t_{2g})-like nature and the particle mainly of Co(e_g)-like nature. $Fe^{II}(t_{2g}) \rightarrow Co^{III}(e_g)$ transitions, corresponding to the optical gap, are located in the 1200-1500 nm range, but have an extremely weak oscillator strength, while additional transitions with CT character are located around 390 nm. In Fig. 4, the measured OD change and the calculated oscillator strength changes between the ground $Co^{III}Fe^{II}$ and the photoinduced $Co^{II}Fe^{III}$ qualitatively agree, with a bleaching of the Co d-d band of the $Co^{III}Fe^{II}$ state (540 nm) and the appearance of two bands below (440 nm) and above (640 nm) in the $Co^{II}Fe^{III}$ state.

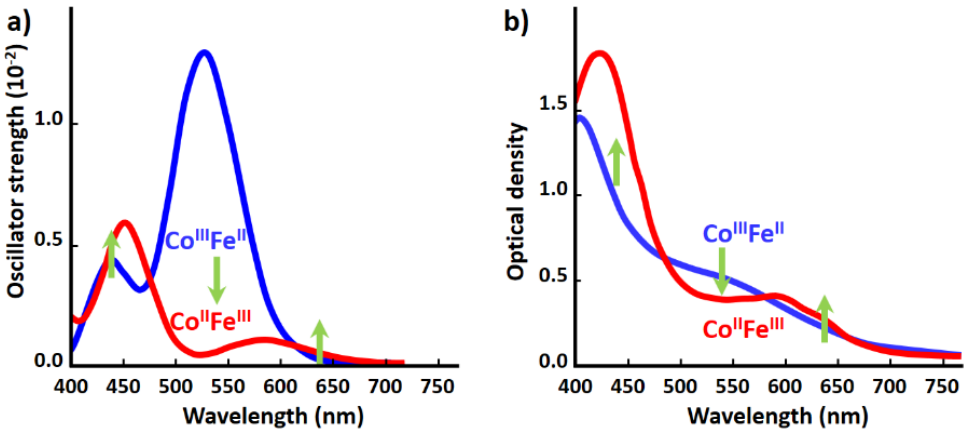

Fig. 4. Calculated oscillator strength (a) and measured OD change after photoexcitation at 10 K (b). The switching from the ground $Co^{III}Fe^{II}$ to the photoinduced $Co^{II}Fe^{III}$ is associated with bleaching of the Co d-d band of the $Co^{III}Fe^{II}$ state (540 nm) and the appearance of two bands below (440 nm) and above (640 nm) in the $Co^{II}Fe^{III}$ state.

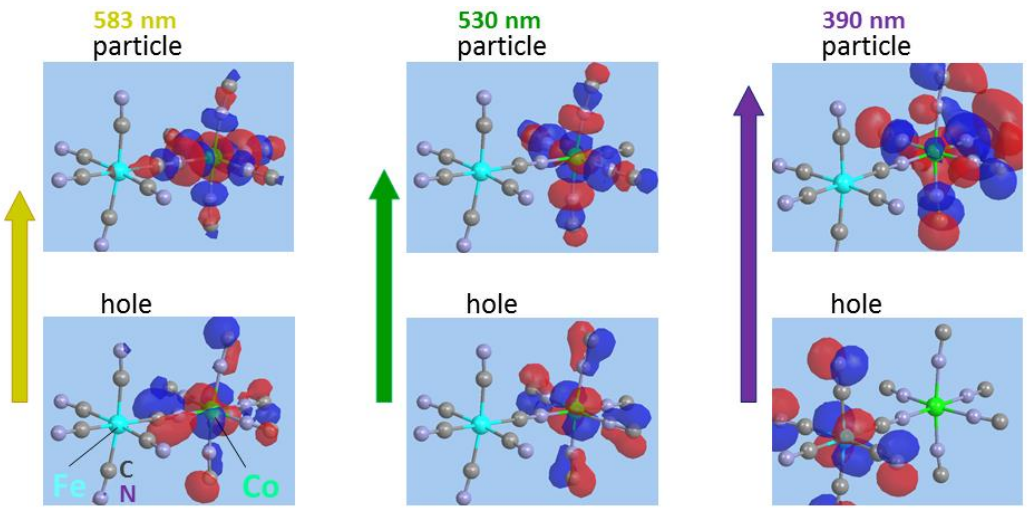

Fig. 5. Natural transition orbitals (NTO) of the $Co^{III}Fe^{II}$ state. NTO of hole and particle for different transitions showing the $Co^{III}t_{2g} \rightarrow e_g$ nature of the transitions in the 530-580 nm range, and the CT $Fe^{II}t_{2g} \rightarrow Co^{III}e_g$ nature of the transition located at 390 nm. C atoms are in grey.

XANES spectral changes

Fig. 6 shows the changes of the XANES spectra of the CoFe nanoparticles, measured at the LCLS around Co and Fe edges (7a and 7b) before and after laser irradiation. The inset of fig. 6a shows the XANES white line before laser irradiation, with maxima at 7725 eV and 7728 eV characteristic of the presence of both Co^{II} and Co^{III} ions, as shown by Bordage [ref 27]. The XANES spectral change demonstrates the photo-conversion from Co^{III} to Co^{II}. Fig. 6c and 6d show the intensity change measured 3 ps (red) after photoexcitation. These are compared to the XANES intensity changes reported by Bleuzen et al (ref 13) during the photoinduced $Co^{III}Fe^{II}$ to $Co^{II}Fe^{III}$ transition under pressure (blue). There are two processes which contribute to spectral changes at the Fe and Co edges : the change of oxidation state due to charge-transfer and the structural reorganization due to the spin transition.

- At the Fe edge, the XANES change is mainly due to CT as there is little structural reorganization in the vicinity of the Fe. The green curve is the spectral change calculated from the ground state, by taking into account the 0.6 eV rigid spectral shift reported by Bleuzen et al (ref 13) after $Co^{III}Fe^{II}$ to $Co^{II}Fe^{III}$ photo-switching. The blue and green curves superpose perfectly, confirming that, at the Fe edge, it is mainly the CT which contributes to the spectral change between $Co^{III}Fe^{II}$ and $Co^{II}Fe^{III}$ states. This spectral shift is mainly characterized by an increase of absorption above 7131 eV and a decrease of absorption below. We attribute the ~1 eV mismatch between Bleuzen's data and our data to a difference in the energy calibration of the instruments used in the two experiments.

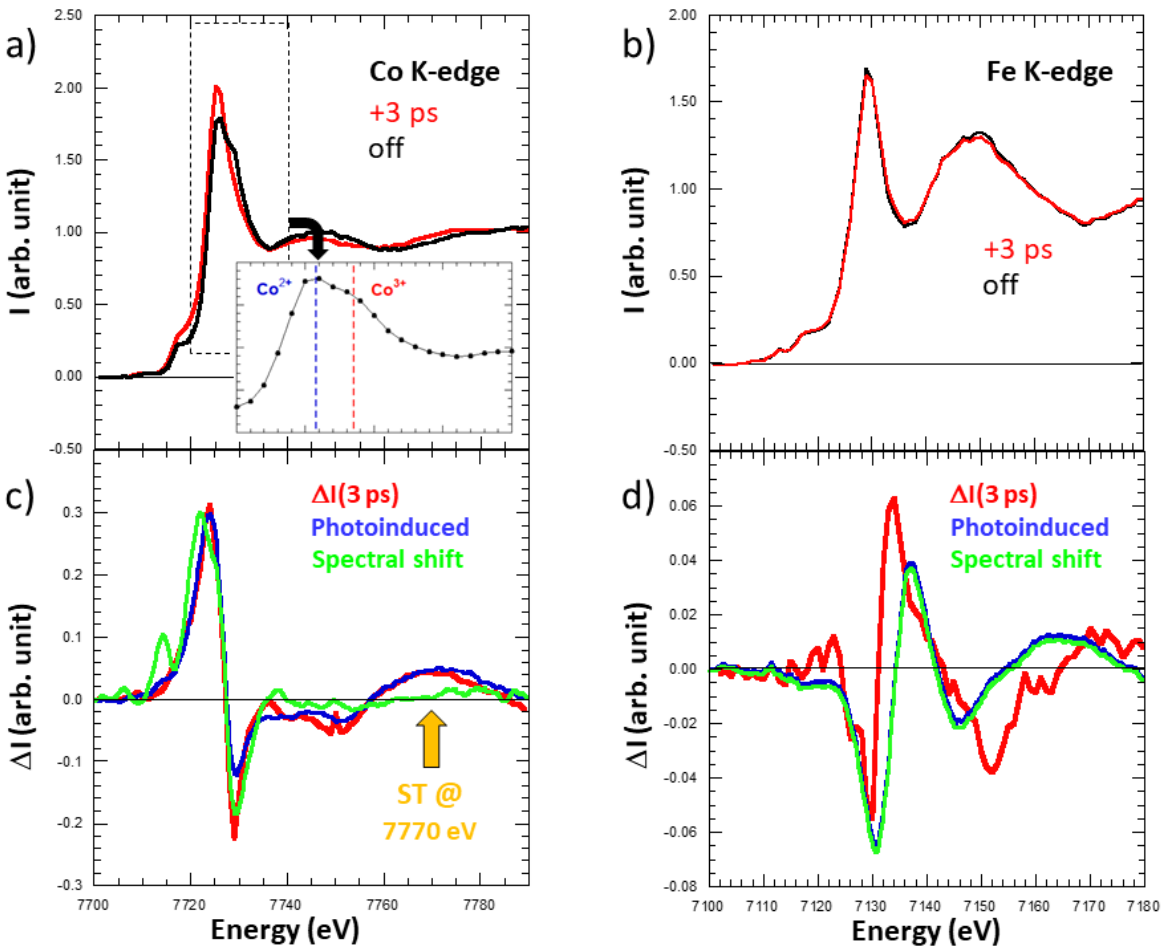

Fig. 6. XANES spectral changes. XANES spectra of the CoFe nanoparticles at the Co and Fe edges **(a,b)**. The inset at the Co edge shows the maxima at 7725 eV and 7728 eV characteristic of Co^{II} and Co^{III} states. XANES intensity change measured at the LCLS around Co and Fe edges 3 ps (red) after photoexcitation **(c,d)**, compared to XANES intensity changes reported by Bleuzen et al (ref 13) during the photoinduced $Co^{III}Fe^{II}$ to $Co^{II}Fe^{III}$ phase transition under pressure (blue). The green curves represent the spectral changes due to CT only and due to rigid spectral shifts (2 eV at the Co edge and 0.6 eV at the Fe edge).

Our time-resolved spectral change data (red curve) provide a satisfying agreement, with absorption increase (resp. decrease) above (resp. below) the isosbestic point around 7131 eV. The difference at higher energy may be due to the inhomogeneous nature of our sample or the partial conversion as in Bleuzen's data the initial and final states correspond to pure $Co^{III}Fe^{II}$ and $Co^{II}Fe^{III}$ states. Another possible explanation for this spectral difference at higher energy is that after 3 ps some torsion remains in the crystal lattice, which may not be equilibrated. Indeed, the lattice expansion timescale is limited to ≃6 ps, as given by the ratio between the sample size (11 nm) and the speed of sound (≃2000 m/s) at which elastic deformation waves propagate. It is therefore likely that the crystal structure is still locally distorted after 3 ps, as indicated by the activation of the torsion mode during the photo-switching process.

- At the Co edge, the spectral change we observe 3 ps after photoexcitation (red curve Fig. 6c) is in very nice agreement with Bleuzen's data (blue), characterizing the photoinduced Co^{III}(S=0) to Co^{II}(S=3/2) transformation.

Data analysis of femtosecond optical pump / X-ray probe and optical pump / probe spectroscopies.

We analyse the data in two steps, with independent fits first and a global fit of the data in a second stage.

For the independent fits of the different XANES time traces, we used a Gaussian function to describe the instrument response function (IRF), $IRF_X(t) = \frac{1}{\sqrt{2\pi}\sigma_X}\exp(-\frac{t^2}{2\sigma_X^2})$, characterized by the Gaussian RMS width σ_X. The fastest time trace was observed at the Co edge (7729 eV), where the measured signal $S_{7729}(t)$ is the convolution of the IRF with the exponential dynamics at positive delays, selected by Heaviside function $H(t)$: $S_{7729}(t) = IRF_X(t) \otimes \left[A_{7729}\left(1 - \exp\left(\frac{-t}{\tau_1}\right)\right).H(t)\right]$.

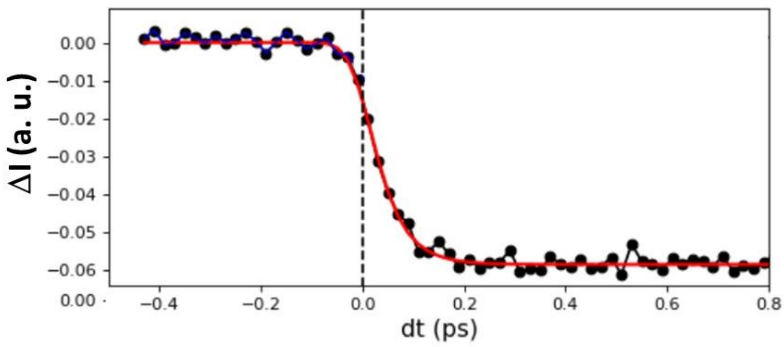

Fig. 7. XANES IRF_X. Fit of the time trace at 7729 eV providing the IRF (σ_X=25(10) fs) and the exponential time constant τ_1=46(11) fs.

From the fit shown in Fig. 7, where the amplitude A_{7729} is a free parameter, we obtained σ_X=25(10) fs and τ_1=46(11) fs. Similar fits at 7770 and 7724 eV also gave an IRF in the 25(10) fs range. The IRF of the XANES experiment was then fixed to σ_X=25 fs for fitting the other XANES time traces. We performed independent fits for each XANES time trace by decomposing the signal into:

- rising components: $R_i(t) = A_i[1 - \exp\left(\frac{-t}{\tau_i}\right)]$

- decaying components: $D_i(t) = A_i \exp(\frac{-t}{\tau_i})$

with characteristic timescales τ_i and amplitudes A_i as free parameters.

Figs. 8a&b show selected fits for which we clearly distinguish different components:

- at the Fe edge, the main component is τ_2≈ 200 fs (203-216 fs range), with an additional τ_3≈ 450 fs (466 fs).

- at the Co edge, the main component is faster with τ_1≈ 50 fs (43-53 fs range). We also observed observe a similar τ_3≈ 450 fs (430-469 fs range). At 7727.1 eV, we fixed τ_2 to 200 fs due to the correlation with τ_3.

We performed similar fits for the OD data (Fig. 8c). However, due to the instrument response function of the OD set-up, IRF_{OD} characterized by $\sigma_{OD} = 80(5)\ fs$, the 50 fs dynamics appears as a step convoluted to the IRF. Here again we find time constants $\tau_3 \approx 450$ fs (414 455 fs range). The damped oscillating component is clearly observed in OD with a frequency $\omega_o \approx 1.65$ THz (period T_o in the 593-657 fs range) with a damping constant $\tau_o \approx 600$ fs (440-853 fs range). For the XANES data, a weak oscillating component is observed in some time traces as well. For XANES and OD data, a slower component needs to be included sometimes through a weak linear contribution, very likely due to a much slower process like the global crystal expansion not resolved here.

All those independent fits evidence that:

- the Co-N bond elongates within $\tau_1 \approx 50$ fs, as independently monitored at 7770 eV through the associated characteristic shift of the first EXAFS feature accompanying the spin transition on the Co.
- the CT occurs within $\tau_2 \approx 200$ fs, as monitored through the associated changes at the Fe edge related to the spectral shift, and also observed for some time traces at the Co edge. 7121 eV also probes a change in the population of Fe d states related to CT.
- an intermediate (INT) state (or several) forms and decays within 200 fs, as clearly observed at the Fe and Co isosbestic points, accompanied by a 450 fs decaying dynamics.
- the oscillating component at $\omega_o \approx 1.65$ THz, corresponding to periods $T_o \approx 600$ fs, is damped with time constant $\tau_o \approx 600$ fs, clearly seen in OD and observed for some XANES data (Fig. 8).

In a second step, we fixed the time constants of the different processes to their characteristic values found from the independent fits: τ_1=50(10) fs, τ_2=200(10) fs and τ_3=450(40) fs. For the oscillating component, we used a damping constant $\tau_o \approx$ 600 fs and a frequency ω_o=1.65 THz. Then we extracted the amplitudes A_i of the contribution of each process in the different time traces as shown in Fig. 9. The fits take into account the convolution with the IRF (σ_X=25 fs for XANES data and σ_{OD} =80 fs for OD data). The global fits of the XANES signals measured at different X-ray energies around the Co and Fe edges and in the OD changes are shown by black lines in the main text in Fig. 2. The time trace at 7131 eV shown in Fig. 9b exhibits a single dynamics (τ_2=200 fs), easily decomposed into two components: an exponential decay due to an intermediate (INT) state (or several) and an exponential increase due to charge transfer (CT):

$$S_{7131}(t) = IRF_X(t) \otimes \left[[A_{INT}\, exp\left(\frac{-t}{\tau_2}\right)].H(t) + \left[A_{CT}\left(1 - exp\left(\frac{-t}{\tau_2}\right)\right).H(t)\right]\right]$$

The INT state, mainly responsible for XANES change around the isosbestic point at the Fe edge (7131 eV), is also responsible for the initial XANES changes at 7129 and 7134 eV.

In addition, the maximum amplitudes around dt=0 of the oscillations show that the equilibrium position is shifted by the spin transition (Fig. 10).

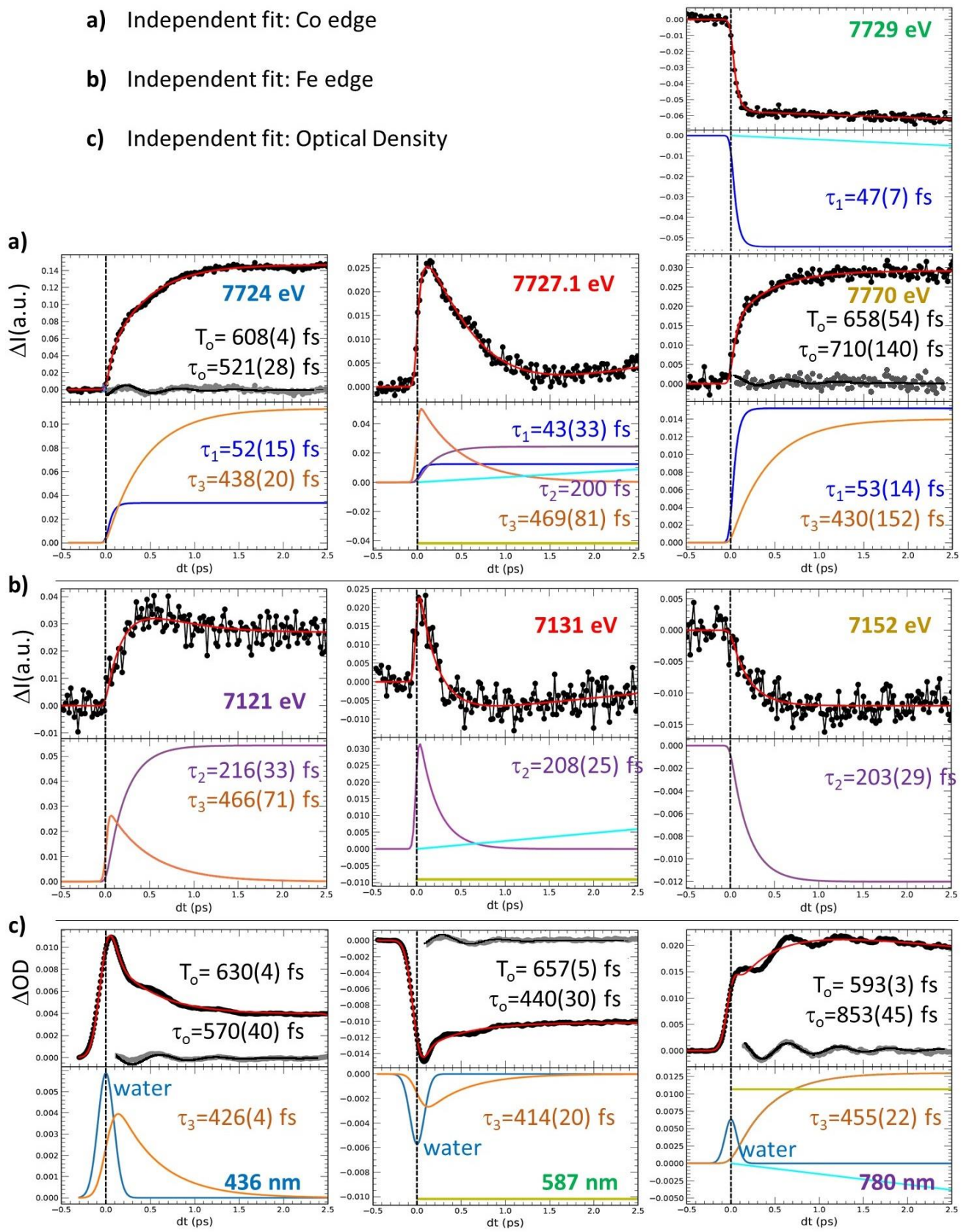

Fig. 8 Independent fit. Independent fits of the time traces of XANES at the Co **(a)** and Fe **(b)** edges and OD **(c)**, resolving different components τ_i to the signals. The residual between the signal and fits with exponential laws evidence damped oscillations of OD and some XANES data with period T_o and damping timescale τ_o. For OD data the water response, exhibiting Gaussian response, was measured independently and included in the fit.

Amplitude/ Probe	a_1 (τ_1=50 fs)	a_2 (τ_2=200 fs)	a_3 (τ_3=450 fs)	a_o (T_o=610 fs) $t_{o=}$ 600 fs
Co 7717 eV	0.0113(3) R	0.034 (5) R	0.025 (3) R	0.0072 (1)
Co 7724 eV	0.024 (2) R	0	0.123 (2) R	0.0088(25)
Co 7727.1 eV	0.012 (4) R	0.024 (18) R	- 0.042 (10) R	0
Co 7729 eV	- 0.056 (3) R	0	0	0
Co 7770 eV	0.0159 (7) R	0	0.0122 (7) R	0.0012 (7) R
Fe 7121 eV	0	0.0667 (6) R	0.032 (4) D	0.004 (2)
Fe 7129 eV	0	- 0.0430 (3) R	- 0.021 (1) D	0.0035 (13)
Fe 7131 eV	0	0.036 (2) D 0.0054 (3) R	0	0
Fe 7134 eV	0	0.049 (6) R	0.037(4) D	0.0028 (18)
Fe 7152 eV	0	- 0.0121 (2) R	0	0
OD 436 nm	0.0040(1)	0.0048 (5) D	0.0051 (2) D	-0.0018 (1)
OD 587 nm	- 0.0109(4)	-0.0023 (7) D	-0.0033 (3) D	0.0015(2)
OD 627 nm	-0.0006(3)	0	-0.0048 (2) D	0
OD 780 nm	0.007(2)	0.010 (1) R	0.010 (1)D	0.0045 (3)

Table 1: Amplitude A_i in the fit of the data of the exponential components with τ_1=50(10) fs, τ_2=200(10) fs, τ_3= 450(40) fs and of the 1.65 THz oscillating component damped within 600 fs. R stands for rising signal in the form $R_i(t) = A_i[1 - \exp\left(\frac{-t}{\tau_i}\right)]$ or decaying signal $D_i(t) = A_i \exp(\frac{-t}{\tau_i})$. Due to the time resolution for OD measurements, the 50 fs component appears as a step convoluted with IRF_{OD}.

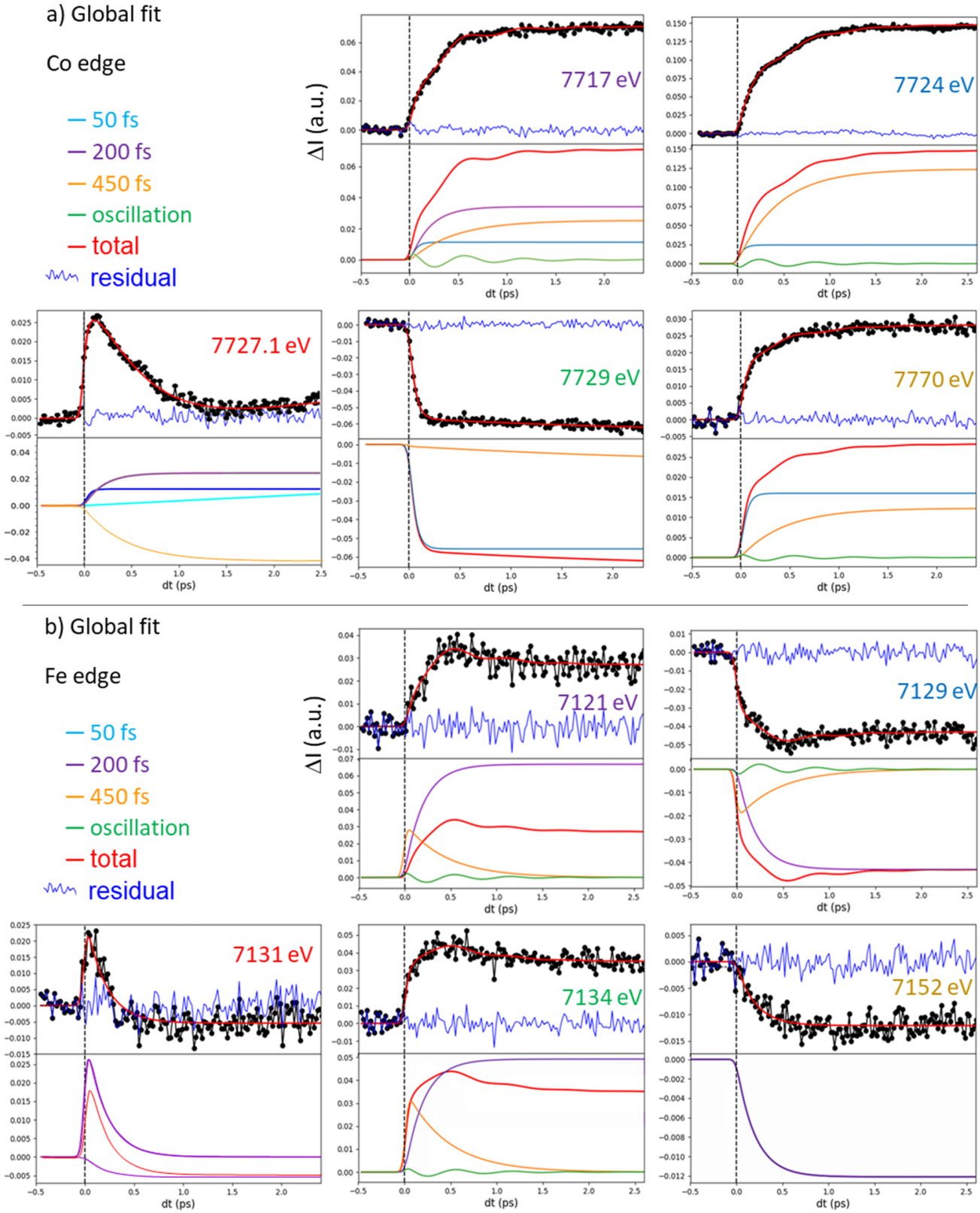

Fig. 9 Global fit of the dynamics. The global fit (black lines) of the data includes exponential components with $\tau_1 \approx 50$ fs (bleu), $\tau_2 \approx 200$ fs (purple) and $\tau_3 \approx 450$ fs (orange) and the oscillating dynamics (green). The global fit highlights the 50 fs dynamics at the Co edge **(a)** and the 200 fs dynamics at the Fe edge **(b)**.

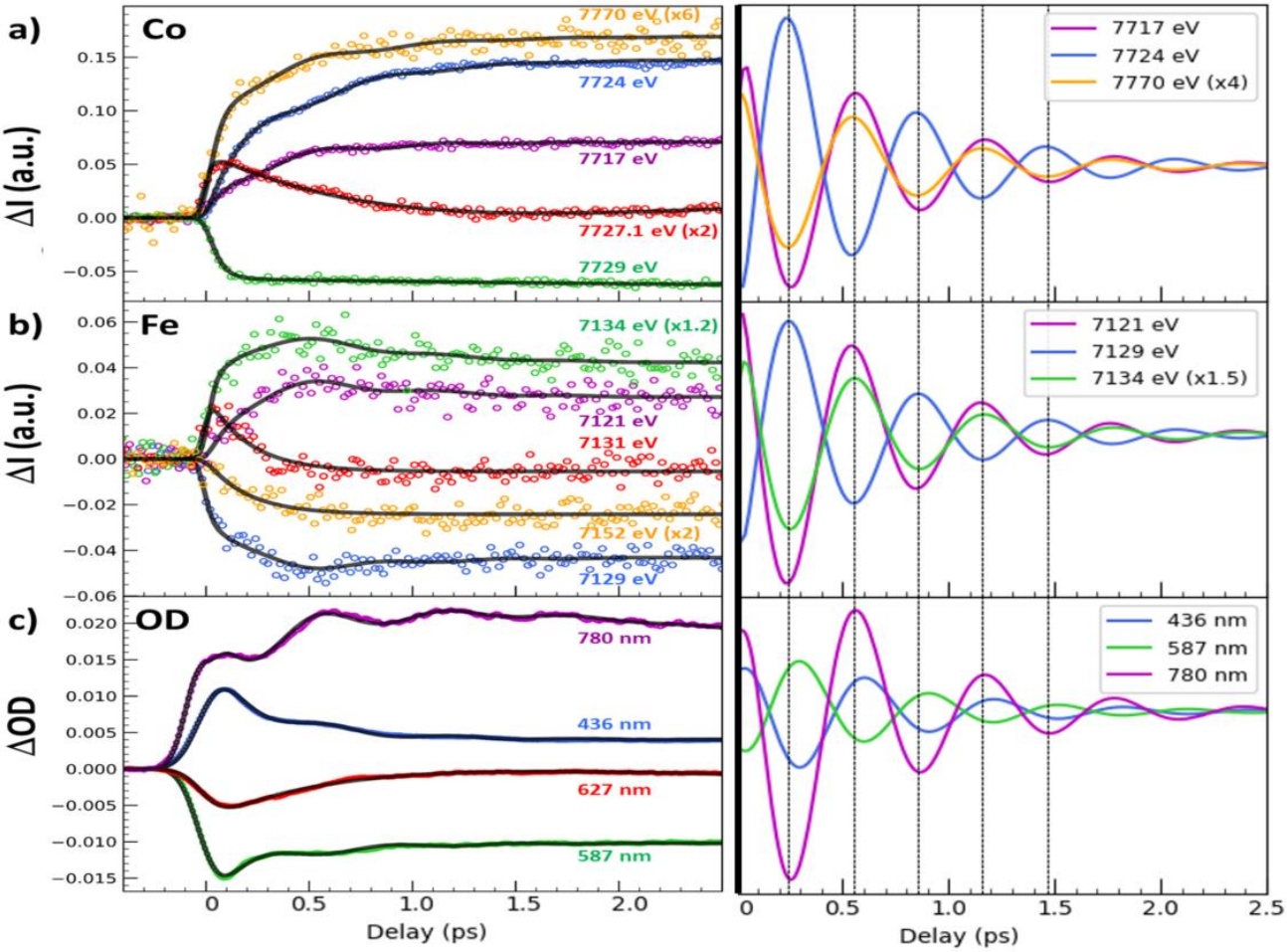

Fig. 10. Oscillating component in the fit of the data. Global fit of the data (left) at the Co edge **(a)**, the Fe edge **(b)** and OD **(c)** with oscillating component (right) showing the maximum amplitude around dt=0 characteristic of a displacive process.